

Room-temperature electrically switchable spinvalley coupling in a van der Waals ferroelectric halide perovskite with persistent spin helix

Lifu Zhang^{1,5}, Jie Jiang^{1,5}, Christian Multunas^{1,2,5}, Chen Ming^{1,5}, Zhizhong Chen¹, Yang Hu¹, Zonghuan Lu², Saloni Pendse¹, Ru Jia¹, Mani Chandra¹, Yi-Yang Sun³, Toh-Ming Lu², Yuan Ping^{1,2}, Ravishankar Sundararaman^{1,2,5} and Jian Shi^{1,2}

Spintronic devices, by harnessing the spin degree of freedom, are expected to outperform charge-based devices in terms of energy efficiency and speed of operation. The use of an electric field to control spin at room temperature has been pursued for decades. A major hurdle that has contributed to the slow progress in this regard is the dilemma between effective control and strong spin relaxation. For example, in a Rashba/Dresselhaus material with strong spin-orbit coupling, although the internal magnetic field could be substantial enough to effectively control spin precession, often, the spin-relaxation time becomes extremely short as a consequence of Dyakonov-Perel scattering. To address this, a persistent spin helix has been proposed in systems with SU(2) symmetry. Here we show the discovery of the persistent spin helix in an organic-inorganic hybrid ferroelectric halide perovskite whose layered nature makes it intrinsically like a quantum well. We demonstrate that the spin-polarized band structure is switchable at room temperature via an intrinsic ferroelectric field. We reveal valley-spin coupling through a circular photogalvanic effect in single-crystalline bulk crystals. The favoured short spin helix wavelength (three orders of magnitude shorter than in III-V materials), room-temperature operation and non-volatility make the hybrid perovskite an ideal platform for understanding symmetry-tuned spin dynamics, towards designing practical spintronic materials and devices that can resolve the control-relaxation dilemma.

omputing paradigms, by harnessing the spin degree of freedom of electrons, characterized by a high switching efficiency and fast processing speed, have been suggested to be promising for addressing the grand challenges that charge-based devices (for example, silicon-based field-effect transistors) are facing in the path towards chip miniaturization¹⁻⁹. In manipulating electron spin, the most common knobs are magnetic field, current and electric field. In microelectronic circuits, the generation of magnetic fields and the scaling of magnetic devices are technically challenging. Current-based approaches suffer from high energy consumption^{5,6}, whereas electric field-based methods are designed to have much lower power consumption than current-based methods and do not have the scaling issue encountered by magnetic-field-based approaches^{3,10,11}. Among a plethora of proposed concepts^{1,3,7,8,10,11}, the Rashba–Dresselhaus effect, a manifestation of the interplay between crystal/device symmetry and spin-orbit coupling (SOC), has been suggested as one of the most feasible mechanisms for designing demanded spintronic devices

When an electron travels in an electric field \overline{E} , the electron experiences an effective magnetic field $\overline{B}_{\text{eff}}$:

$$\vec{B}_{\text{eff}} \sim \frac{\vec{p} \times \vec{E}}{m_0 c^2},$$
 (1)

where m_0 is the mass of the electron, c is the speed of light and \vec{p} is the electron momentum. With $\vec{B}_{\rm eff}$, derived from the Dirac equation, the interaction between the orbital and spin degrees of freedom can be expressed as 13,14

$$\mathbf{H}_{SOC} = \frac{-\hbar}{4m_o^2 c^2} [\mathbf{p} \times (\nabla V)] \cdot \mathbf{\sigma}, \tag{2}$$

where ħ is the reduced Planck's constant, p is the momentum operator, V is the potential and σ is the Pauli vector. In solid crystals lacking inversion symmetry (for example, induced by an external electric field, asymmetric doping or intrinsic crystal symmetry), Rashba and Dresselhaus revealed that H_{SOC} could lead to a spin-polarized electronic band structure (that is, valley-spin locking)15-17. The resulting effective Rashba or Dresselhaus fields have been proposed as the spin precession force in the framework of spin transistors (for example, in the Datta-Das spin transistor). In the pursuit of ideal materials or structures in which to realize such spin transistors, a couple of required features are proposed. The first is the existence of the persistent spin helix, a spin density wave with conserved spin phase and amplitude immune to spin-independent scattering (here, $[\mathbf{H}_{PSH}\mathbf{R}] = 0$, where \mathbf{H}_{PSH} is the Hamiltonian of the materials or structures hosting the persistent spin helix and R is an arbitrary spin rotation operator. This is also known as SU(2)symmetry. This allows operation of the spin transistor in a

¹Department of Materials Science and Engineering, Rensselaer Polytechnic Institute, Troy, NY, USA. ²Department of Physics, Applied Physics, and Astronomy, Rensselaer Polytechnic Institute, Troy, NY, USA. ³State Key Lab of High-Performance Ceramics and Superfine Microstructure, Shanghai Institute of Ceramics, Chinese Academy of Sciences, Shanghai, People's Republic of China. ⁴Department of Chemistry and Biochemistry, University of California, Santa Cruz, CA, USA. ⁵These authors contributed equally: Lifu Zhang, Jie Jiang, Christian Multunas. [™]e-mail: yuanping@ucsc.edu; sundar@rpi.edu; shij4@rpi.edu

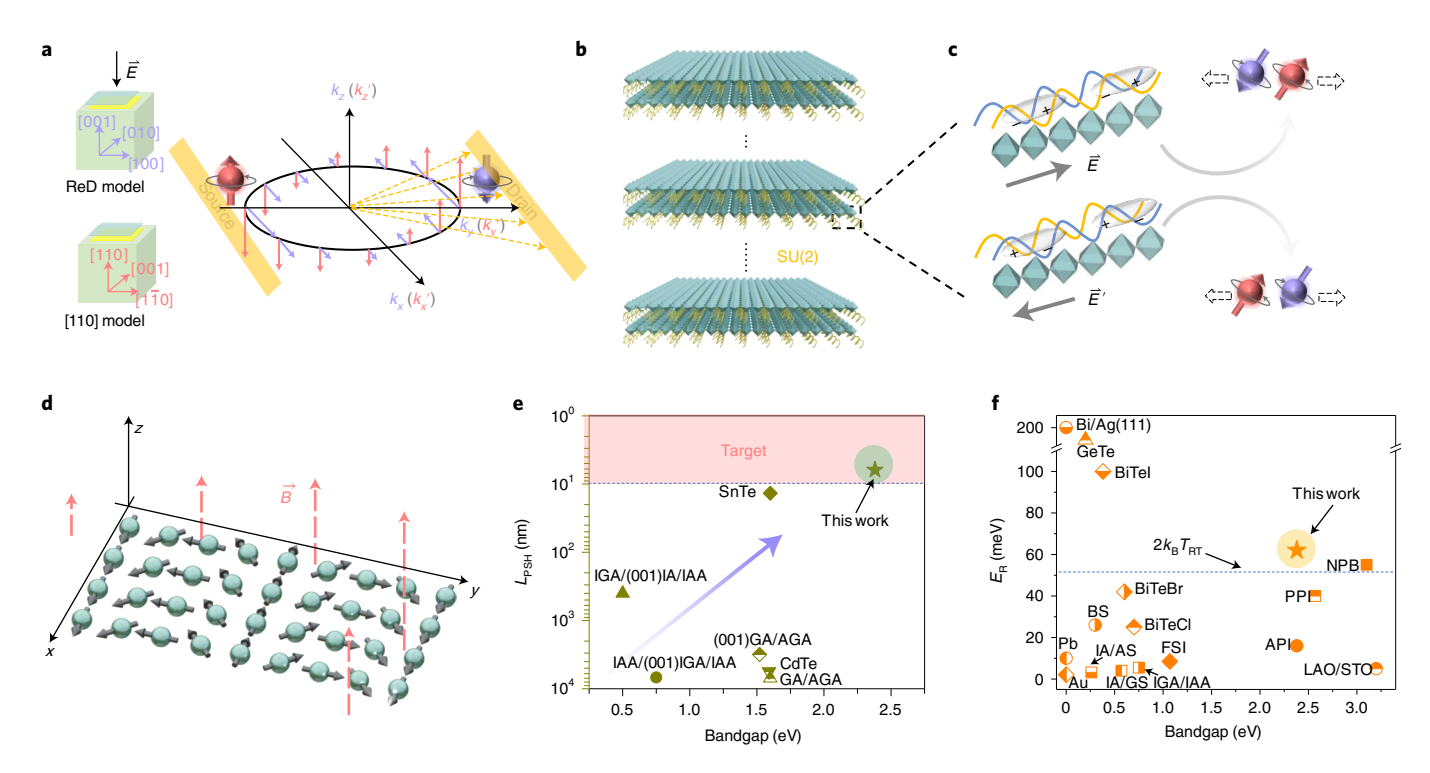


Fig. 1 | The proposal of natural multilayer quantum-well-like bulk crystals with persistent spin helix. **a**, Two major quantum well models for formation of the persistent spin helix. The light blue arrows (ReD model) and light red arrows ([110] model) on the right panel represent the net B. **b**, A natural multilayer quantum-well-like material hosting the SU(2) symmetry-protected persistent spin helix. **c**, Under illumination by circularly polarized lights, excited electrons with spin up/down will move along opposite directions (perpendicular to E and E) due to valley-photon locking, and the travelling direction is reversed once the polarization state is switched by E or E. **d**, A schematic of the persistent spin helix formed in the x-y-plane (in-plane). **e**, Summarized wavelengths of the persistent spin helix L_{PSH} for materials and structures that have been experimentally synthesized/fabricated. Filled symbols represent theoretically computed values and the others are experimental data. **f**, Summarized Rashba splitting energy E_R of typical Rashba and Dresselhaus materials/structures versus their bandgaps. Filled symbols represent theoretically predicted values and the others are experimental values. IGA/(001)IA/IAA, $In_{0.53}Ga_{0.47}As/(001)InAs/In_{0.52}Al_{0.48}As$; (001) $In_{0.53}Ga_{0.47}As/(001)IGA/IAA$, $In_{0.53}Ga_{0.47}As/(001)IGA/IAA$, $In_{0.52}Al_{0.48}As$; (001) $In_{0.53}Ga_{0.47}As/(001)GaAs/AlGaAs$; BS, Bi₂Se₃; PPI, (PEA)₂PbI₄, where PEA is phenethylammonium; API, (AMP)₂PbI₄, where AMP is 4-(aminomethyl)piperidinium; NPB, (NEA)₂PbBr₄, where NEA is 1-(1-naphthyl)ethylamine; FSI, (NH₂CHNH₂)SnI₃; LAO/STO, LaAIO₃/SrTiO₃; IA/GS, InAs/GaSb; IA/AS, InAs/AISb; IGA/IAA, $In_{0.52}Al_{0.48}As$. The parameter B with the half arrow denotes the magnetic field.

non-ballistic regime, as the existence of the persistent spin helix naturally suppresses spin relaxation through Dyakonov–Perel scattering. The second is the existence of strong Rashba or Dresselhaus fields for short precession-channel operations and large splitting energy among spin-polarized band structures.

To enable the persistent spin helix, two major approaches have been adopted. In a (001)-oriented quantum well with zinc blende structure, a careful balance between Rashba and Dresselhaus contributions has to be achieved (in Fig. 1a, net B is indicated by light blue arrows and has a linear dependence on k_y). Another approach for producing a unidirectional field with a linear dependence on k_y that hosts the persistent spin helix is through device structure engineering in a III–V quantum-well system (for example, in a device with C_{2y} point group, with the C_2 axis aligned horizontally, with [110] along the out-of-plane direction). Such a design does not require a delicate balance between the Rashba and Dresselhaus contributions but naturally leads to a symmetry-protected persistent spin helix (indicated by light red arrows in Fig. 1a). Implementation of these two methods has been successfully achieved in III–V quantum-well systems.

Despite substantial progress in III–V spintronics, a few challenges remain. First, due to the stringent requirements regarding the balance of fields and/or device symmetry, III–V materials and devices require great efforts in terms of materials growth and

processing. Second, the wavelength of the persistent spin helix of III–V materials is usually too long, indicating an extremely long procession length (a few micrometres for GaAs) and limiting applications towards device miniaturization. Third, the energy splitting in the spin-polarized band structure is too small for device operation at room temperature.

In this Article we design the required persistent spin helix through a van der Waals material with required symmetry whose electronic structure is intrinsically like a quantum well. As shown in Fig. 1b,c, by using a ferroelectric organic–inorganic hybrid halide perovskite with a $C_{2\nu}$ point group, a van der Waals structure along the out-of-plane direction and with the C_2 axis aligned horizontally along the x direction, we expect to achieve an effective field as follows (details of the theoretical analysis are provided in Supplementary Discussion 1):

$$\vec{B}_{\rm eff}(\vec{k}) = \alpha' k_y \hat{z},\tag{3}$$

where α' denotes the strength of SOC containing ferroelectric polarization, and k_y is the crystal momentum along the y direction. This field is unidirectional in hosting the SU(2) symmetry-protected persistent spin helix, which is very similar to those reported in III–V systems. The material in our work provides a few advantages over

III–V or other related materials: (1) it has a much higher Rashba coefficient than III–V materials, thus making the wavelength of the persistent spin helix shown in Fig. 1d extremely short (three orders of magnitude shorter than for the III–V materials shown in Fig. 1e); (2) the device structure is free of the conventional quantum well form required by III–V or other materials, with strong interlayer coupling along the out-of-plane directions^{18,19}; (3) the hybrid halide perovskite is ferroelectric at room temperature, allowing non-volatile switching of the persistent spin helix and making it possible to develop an energy-efficient ferroelectric spin transistor.

In this Article the halide perovskite material we use is (4,4-DFPD)₂PbI₄, where 4,4-DFPD is 4,4-difluoropiperidinium (details of its crystal structure and symmetry are discussed in later sections). Figure 1e summarizes the wavelength values of the persistent spin helix L_{PSH} for most known materials and structures. To meet the demand for device miniaturization, L_{PSH} must be a few nanometres or shorter. The L_{PSH} of our halide perovskite material (4,4-DFPD)₂PbI₄ is 6.2 nm, whereas most other materials have much longer $L_{\rm PSH}$ values 18,20-23. It is noted that our material is so far the only known one that has $L_{PSH} < 10 \text{ nm}$. In addition to L_{PSH} , another parameter that determines the performance of a Rashba-type spintronic transistor is the Rashba splitting energy (E_R) . In Fig. 1f we summarize E_R for most known Rashba/Dresselhaus materials and structures (see Supplementary Information for references). It can be seen that our material has an E_R of 62 meV, which is much higher than in the III-V materials (<10 meV). It is also much larger than $k_{\rm B}T_{\rm RT}$ ($k_{\rm B}$, Boltzmann constant; $T_{\rm RT}$ room temperature), making room-temperature operation feasible. The exceptional values of $L_{\mbox{\tiny PSH}}$ and E_R in $(4,4-DFPD)_2PbI_4$, together with its ferroelectricity, make it a promising Rashba spintronic material.

The material (4,4-DFPD)₂PbI₄ has an organic-inorganic layered orthorhombic structure that features monolayers of corner-shared PbI₆ octahedra in the a-b plane sandwiched by the out-of-plane neighbouring 4,4-DFPD cations (Fig. 2a). The space group of its ferroelectric phase is B2cb (point group $C_{2\nu}$)²⁴. The crystal has three point group symmetry elements: a two-fold rotational symmetry element C_2 with the rotation axis along a (Supplementary Fig. 1b), and two mirror symmetry elements M_{ab} (Supplementary Fig. 1a) and M_{ac} . These three symmetry elements, together with the quantum-well structure, guarantee the presence of a unidirectional magnetic field with a linear dependence on k_y and the existence of persistent spin helix (more details are provided in Supplementary Discussion 1). In (4,4-DFPD)₂PbI₄, the 4,4-DFPD organic cations align along the a axis in a head-to-tail manner (right part of Fig. 2a and Supplementary Fig. 1), making a the ferroelectric polarization direction. Its ferroelectricity allows the switching of the direction of unidirectional fields and thus the persistent spin helix vector.

Figure 2b shows the spin-polarized electronic band structure of ferroelectric (4,4-DFPD)₂PbI₄ as calculated by density functional theory (DFT; the full band structure and analysis of the projection of the total angular momentum are shown in Supplementary Fig. 2). Consistent with our symmetry analysis, a large spin-polarized band splitting occurs along the G-Y direction at both the conduction band minimum (CBM; Fig. 2b, inset) and valence band maximum (VBM). For CBM and VBM, $E_R = 62 \text{ meV}$ and 22 meV, respectively, with electron spin aligned along the *c* (marked by the red lines) or -c (by blue lines) directions. The momentum offset k_R for CBM is found to be $\frac{\pi}{6.2 \text{ nm}}$, which is one of the highest among known Rashba materials. At k_R , the spin momentum $\langle S_z \rangle$ at the VBM reaches $\pm 0.47\hbar$ and $\langle S_z \rangle$ at the CBM reaches $\pm 0.42\hbar$, both of which are close to the maximum/minimum value of $\pm 0.5\hbar$. We also calculated the optical probability of transition for circularly polarized light (that is, left circularly polarized (LCP, σ^-)) near the band edge. The probability of transition of σ^- from VBM to CBM at the $-k_v$ valley, involving $m_{i_{\perp}VBM} = -1/2$ to $m_{i_{\parallel}CBM} = +1/2$, reaches 97.5%, whereas it is only 2.5% in the $+k_v$ valley (note that $m_{i_VBM} = -1/2$

and $m_{j_CBM} = +1/2$ are approximations based on the computed density of states near the VBM and CBM shown in Supplementary Fig. 3). These values are also close to the ideal case where 100% and 0% are expected, respectively.

Figure 2c displays the spin texture of $(4,4\text{-DFPD})_2\text{PbI}_4$ near the CBM in the k_x-k_y plane. The lifting of spin degeneracy gives rise to two opposite valleys carrying opposite spins: the valley coloured in red is for spin-up states (along the c direction) and the one in blue for spin-down states (along the -c direction). More information about spin texture near the CBM and VBM in different k spaces is provided in Supplementary Figs. 4 and 5. Figure 2d,e displays the calculated effective magnetic field near the CBM in the k_x-k_y plane and k_y-k_z plane, respectively. As we can see, B_{eff} is along the $+k_z/-k_z$ direction in the $+k_y/-k_y$ valley, and its magnitude increases when $|k_y|$ increases. A numerical mapping of B_{eff} in the k space near the CBM is shown in Fig. 2f. It is noteworthy that there is almost zero projection of B_{eff} in the k_x and k_y plane. The linear

relationship of calculated $\overrightarrow{B}_{\rm eff}$ with k_y ($\overrightarrow{B}_{\rm eff}=1.99\times10^{-6}$ (T m) $k_y\hat{z}$ by DFT) confirms our theoretical analysis resulting in equation (3) through the symmetry argument (more information is provided in Supplementary Discussion 2). Similar observations can be made near the VBM, as displayed in Fig. 2g,h. Specifically for the VBM, $\overrightarrow{B}_{\rm eff}$ is along the $-k_z/+k_z$ direction in the $+k_y/-k_y$ valley. Based on the computational results, a persistent spin helix wave with $L_{\rm PSH}$ of around 6.2 nm ($L_{\rm PSH}=\pi/k_{\rm R}$) can thus be expected, as shown in Fig. 2i, where the spin precession occurs in the a-b plane with the effective magnetic field along the c direction and its wave vector pointing in the b or -b direction. More details on the spin and effective magnetic field structures of the relaxed (4,4-DFPD)₂PbI₄ crystals are presented in Supplementary Figs. 6–8.

In this Article we use the single-crystalline form (unless otherwise specified) of (4,4-DFPD)₂PbI₄ to reveal its optoelectronic and opto-spintronic properties. Synthesis of the single-crystalline (4,4-DFPD)₂PbI₄ was carried out as follows. PbI₂ and 4,4-difluoropiperidinium hydrochloride were first fully dissolved in HI aqueous solution, then the new solution was slowly cooled to room temperature for precipitation of the crystals (more details are provided in the Methods). Figure 3a shows the X-ray diffraction (XRD) spectrum of a (4,4-DFPD), PbI4 single crystal, in which a series of (00n) peaks can be detected that indicate that the out-of-plane direction is along the c axis. The insets of Fig. 3a show optical images of the synthesized (4,4-DFPD)₂PbI₄ single crystals and a typical (4,4-DFPD), PbI4 crystal with a length of more than 1 cm. The polarization direction (a axis) is parallel to the long edge, as verified by electron backscatter diffraction (EBSD) analysis (Supplementary Fig. 9).

Figure 3b shows the room-temperature photoluminescence (PL) spectra of a (4,4-DFPD)₂PbI₄ single crystal and the room-temperature absorption spectrum of a (4,4-DFPD)₂PbI₄ thin film fabricated by a spin-coating approach in which the coating solution was prepared by dissolving as-synthesized (4,4-DFPD)₂PbI₄ crystals in dimethylsulfoxide (DMSO; details are provided in the Methods). The absorption spectrum shows that (4,4-DFPD)₂PbI₄ has a strong excitonic transition at 2.38 eV, followed by a band transition with an onset at ~2.6 eV (see the Tauc plot in Supplementary Fig. 10). The exciton binding energy is estimated to be ~220 meV (assuming the excitonic peak is the 1s state), which is consistent with the two-dimensional (2D) nature of our (4,4-DFPD)₂PbI₄ crystal. This value is also within the ranges generally observed in many other low-dimensional layered halide perovskites^{25,26}. The room-temperature PL peak position is close to the excitonic absorption peak, suggesting that the PL is dominated by the excitonic transition.

The temperature-resolved PL spectra of a $(4,4\text{-DFPD})_2\text{PbI}_4$ single crystal at temperatures from $120\,\text{K}$ to $250\,\text{K}$ are displayed in Fig. 3c (the window of $120\text{--}250\,\text{K}$ was chosen so we could

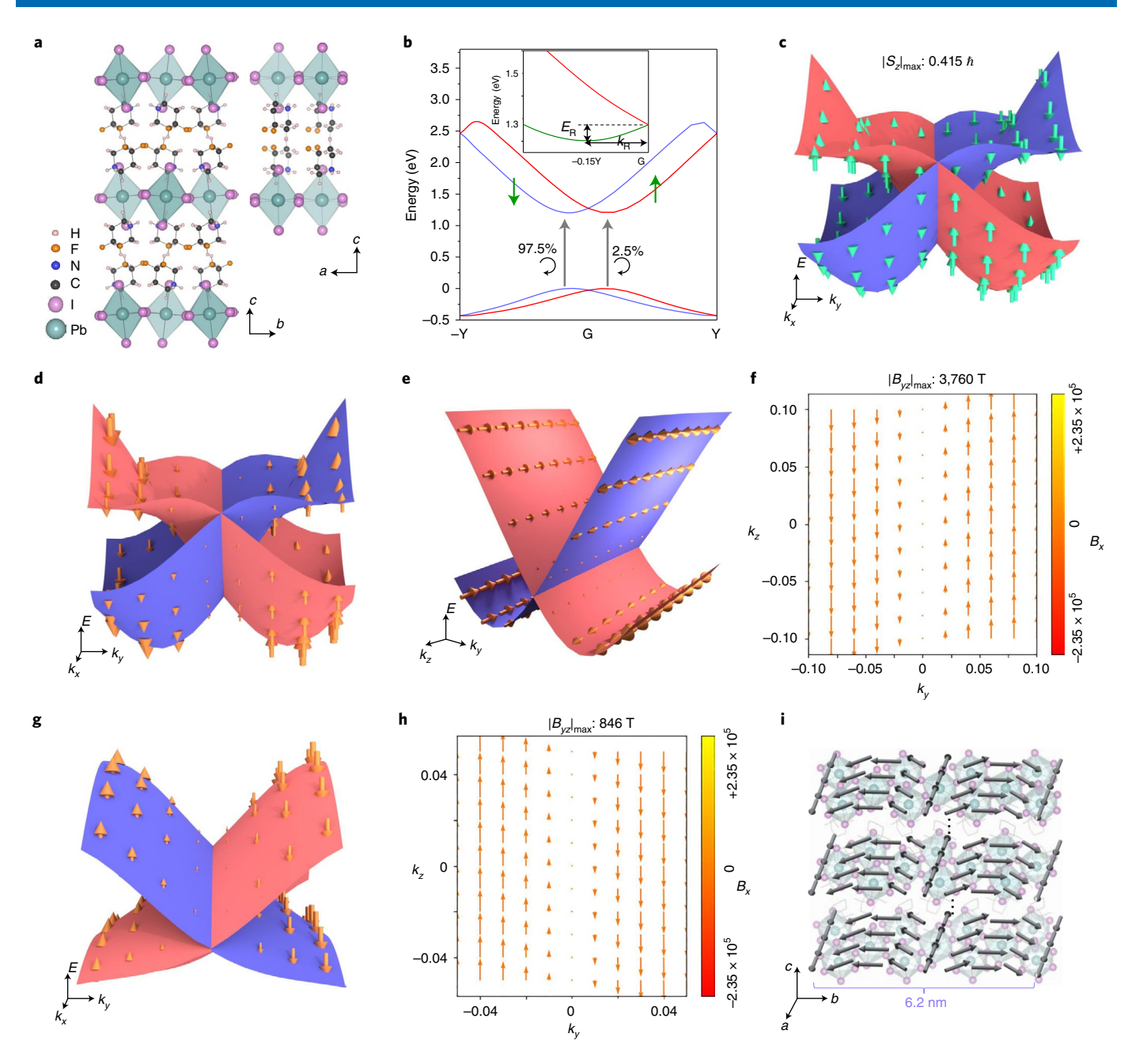


Fig. 2 | Theoretically calculated spin and effective magnetic field structures of $(4,4\text{-DFPD})_2\text{Pbl}_4$ predicted to host the persistent spin helix. **a**, The crystal structures of $(4,4\text{-DFPD})_2\text{Pbl}_4$ from the view of the a axis (left) and b axis (right). **b**, Spin-polarized band structure of ferroelectric $(4,4\text{-DFPD})_2\text{Pbl}_4$ along the G-Y direction with SOC considered. Red/blue colours represent projected spin values along the z direction (z axis) (approximately $+1/2\hbar/-1/2\hbar$). Inset: band structure near the CBM. **c**, Spin texture of $(4,4\text{-DFPD})_2\text{Pbl}_4$ near the CBM in k_x and k_y space. k_x , $k_y \in [-0.1a_0^{-1}, 0.1a_0^{-1}]$, where a_0 is the Bohr radius. The size and direction of the green arrows represent the value and direction of spins, respectively. **d**,**e**, Effective magnetic field B_{eff} near CBM in the \underline{k}_x and k_y space (**d**) and k_y and k_z space (**e**). \underline{k}_x , k_y , $k_z \in [-0.1a_0^{-1}, 0.1a_0^{-1}]$. The size and direction of brown arrows represent the magnitude and direction of B_{eff} , respectively. **f**, Numerical mapping of B_{eff} in the k space near the CBM. Units for B_{eff} , T. **g**, Effective magnetic field B_{eff} near the VBM in k_x and k_y space. k_x , $k_y \in [-0.05a_0^{-1}, 0.05a_0^{-1}]$. **h**, Numerical mapping of B_{eff} in k space near the VBM. Units for B_{eff} , T. **i**, The linear dependence of B_{eff} on k_y guarantees the existence of the persistent spin helix, with its wave vector and the precession axis along b and c directions, respectively, of $(4,4\text{-DFPD})_2\text{Pbl}_4$. The polarization direction [100]/[100] thus determines the precession direction.

minimize crystal damage during laser illumination at high temperatures). The excitonic emission peak exhibits a blueshift of $22\,\text{meV}$ (from 2.349 to $2.371\,\text{eV}$) when increasing the temperature from $120\,\text{K}$ to $250\,\text{K}$ (Fig. 3d). This blueshift of the bandgap can be well explained by the ionic nature of the Pb–I bonds, which carry a net positive deformation potential^{27,28}. This is also widely observed in most halide perovskites^{29,30}. By including the Fröhlich interaction³⁰,

the evolution of the full-width at half-maximum (FWHM) of PL peaks was further fitted, as shown in Supplementary Fig. 11. The estimated charge-carrier–LO-phonon coupling strength γ_0 is equal to 48.7 meV, which is comparable to the value found in other 2D layered halide perovskites^{31,32}.

Figure 3e shows the time-resolved PL (TRPL) spectra of the (4,4-DFPD)₂PbI₄ crystal at temperatures from 120 K to 240 K.

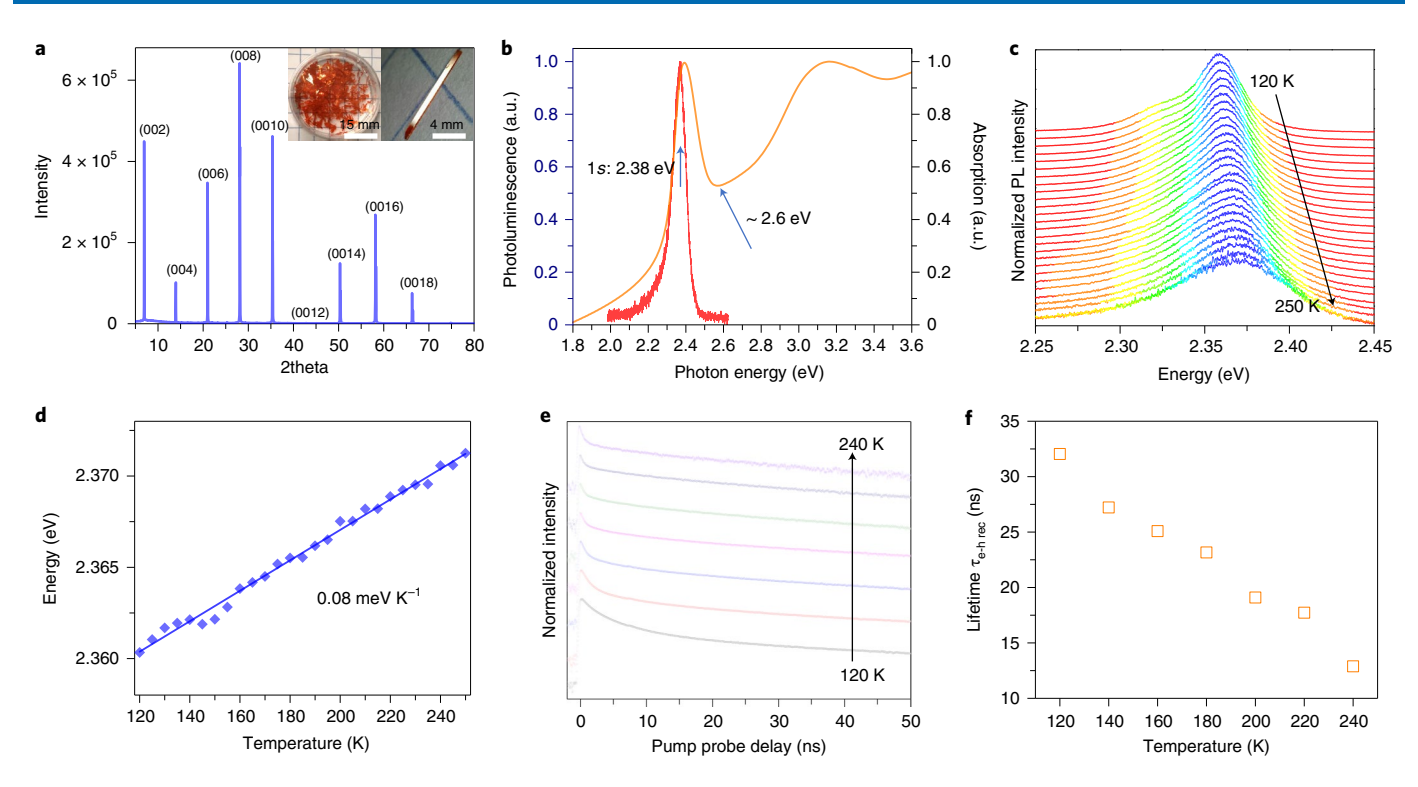


Fig. 3 | Structural and optical properties of (4,4-DFPD)₂**Pbl**₄**.a**, XRD spectrum of a (4,4-DFPD)₂Pbl₄ single crystal. Inset: optical images of (4,4-DFPD)₂Pbl₄ single crystals. **b**, Absorption spectrum of a (4,4-DFPD)₂Pbl₄ thin film (right vertical axis) and PL of a (4,4-DFPD)₂Pbl₄ single crystal (left vertical axis) measured at room temperature. **c**, Temperature-resolved PL spectra of a (4,4-DFPD)₂Pbl₄ single crystal with a fluence of $0.008\,\mu\text{J cm}^{-2}$. The temperature range is from 120 K to 250 K with steps of 10 K. **d**, Position of the exciton peak of (4,4-DFPD)₂Pbl₄ in **c** as a function of temperature. **e**, Temperature-dependent time-resolved PL of (4,4-DFPD)₂Pbl₄ with a fluence of $0.008\,\mu\text{J cm}^{-2}$. The detection wavelength is 525 nm. The temperature range is from 120 K to 240 K with steps of 20 K. **f**, Electron-hole recombination lifetime $\tau_{\text{e-hec}}$ as a function of temperature, fitted from the curves in **e**.

The TRPL spectra can be well fit by a two-exponential function reflecting the surface and bulk contributions for electron–hole recombination. Figure 3f shows the plot of bulk electron–hole recombination lifetime $\tau_{\rm e-hrec}$ versus temperature. At higher temperatures, a shorter bulk $\tau_{\rm e-hrec}$ is observed due to phonon scattering^{32,33}. At 120 K, the bulk $\tau_{\rm e-hrec}$ reaches 32 ns, which is one of the highest among most 2D halide perovskites^{32,34,35} at a similar temperature. When the fluence of the incident light decreases, the bulk $\tau_{\rm e-hrec}$ at 240 K increases, which reflects the nature of the biomolecular electron/hole recombination reaction²⁹(Supplementary Fig. 12).

The optical selection rule involving circularly polarized light³⁶ can be formulated as $\langle f|\hat{\mathbf{c}}\cdot\hat{\mathbf{r}}|i\rangle = \langle n_f, l_f, m_f|\hat{\mathbf{c}}\cdot\hat{\mathbf{r}}|n_i, l_i, m_i\rangle$ in which $\langle f|\hat{\epsilon}\cdot\hat{\mathbf{r}}|i\rangle$ is non-zero only when $m_f-m_i=\pm 1$ and $l_f-l_i=\pm 1$, where $\hat{\epsilon}$ is the polarization vector, $\hat{\mathbf{r}}$ is the position vector operator, $|f\rangle$ and $|i\rangle$ represent two eigenstates, and n, l and m are principal quantum number, azimuthal quantum number and magnetic quantum number, respectively. Because the ferroelectric (4,4-DFPD)₂PbI₄ crystal has a strong spin-polarized band structure with large energy splitting along the b direction, valley-dependent absorption will occur for circularly polarized light with opposite angular momenta. This would lead to a non-zero net charge current along the valley-spin locking direction (b direction) when only one type of circularly polarized illumination is applied. Along the polar direction where spin degeneracy still holds, zero net charge is expected. Such an effect is named the circular photogalvanic effect (CPGE).

To verify the theoretical analysis above, two types of device were designed and fabricated, as sketched in Fig. 4a,d. In Fig. 4a, the direction for measuring the photocurrent is along the polar axis (*a* axis) of the crystal. In Fig. 4d, the direction for measuring the photocurrent is along the direction where spin-polarized band

splitting occurs (b axis). The incident angle α of the laser light is with reference to the z axis (parallel to the c axis of the crystal), whereas the azimuthal angle θ is with reference to the y axis (parallel to the b axis of the crystal) and φ is the angle between the fast axis of the quarter-wave plate (QWP) and the polarization direction of the incident light. When φ is tuned from 0 to 45 to 90 to 135°, the polarization of the light after the QWP changes from linearly polarized (σ°) to right circularly polarized (RCP, σ^{+}) to σ° and then to LCP (σ -). Simple optoelectronic measurements show that the (4,4-DFPD)₂PbI₄ crystal has reasonable photoconductivity (Supplementary Figs. 13 and 14). In the device shown in Fig. 4a, after electrical poling along the polar direction (in the P' state, for example), the zero-bias photocurrent was collected under continuous illumination of a 405-nm laser with light polarization modulated (Fig. 4b). As we can see, there is no difference in photocurrent when the light switches from σ^+ to σ^- , consistent with our theoretical and computational analysis: because there is no spin splitting along the polar direction (Fig. 4c), incident light, either RCP or LCP, will excite equal numbers of electrons with opposite momenta (grey region, Fig. 4c), leading to a σ^+/σ^- -independent photocurrent along the a axis. In the device in Fig. 4d, the crystal was first electrically poled into the P' state along the a direction (the same condition as in Fig. 3a), and then the zero-bias photocurrent was collected along the b direction. According to the result shown in Fig. 4e, a notable CPGE signal is detected along the b axis (there is a substantial difference of photocurrents between LCP and RCP). As illustrated in Fig. 4f, with an electron as an example, due to the asymmetric distribution of momentum for the excited electrons when the excitation is either σ^+ or σ^- , a net short-circuited current I_1 or I_2 is generated. Besides the CPGE current associated with circularly polarized light, there is also spin-independent photocurrent when the

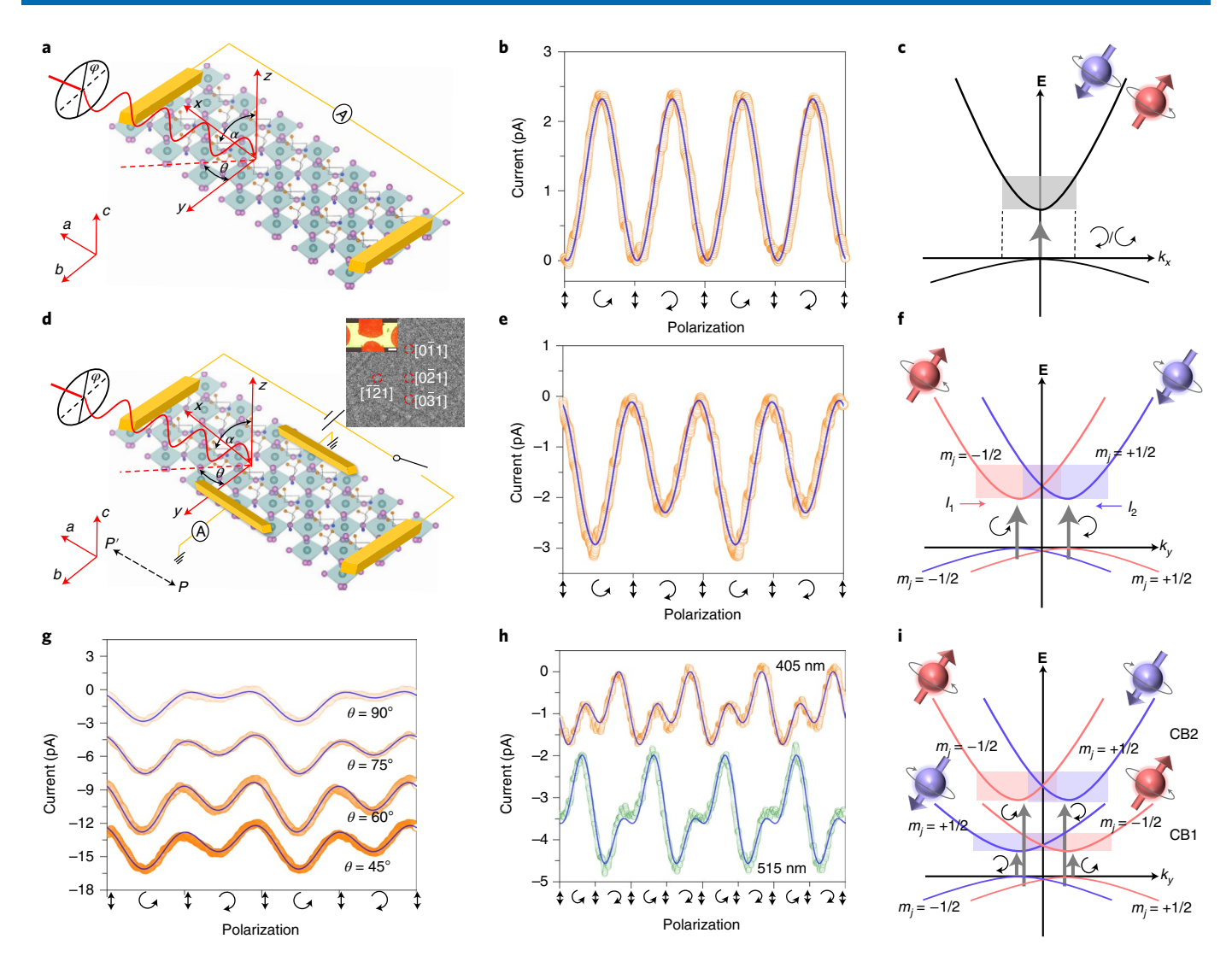


Fig. 4 | **Light helicity-dependent photocurrent. a**, A schematic of the two-terminal device with photocurrent measured along the *a* axis. **b**, Zero-bias photocurrent of a typical device in **a**, which is measured under the illumination of a 405-nm laser with light polarization modulated following the sequence $\sigma^{\circ} \rightarrow \sigma^{+} \rightarrow \sigma^{\circ} \rightarrow \sigma^{-}$ for two periods. (4,4-DFPD)₂Pbl₄ is poled into the P' state beforehand. The incident angle α is -45° and the azimuthal angle θ is 90°. **c**, Proposed scheme of σ^{+}/σ^{-} -induced electron-hole generation along the G-X valley. **d**, A four-terminal device with poling direction along the *a* axis and current detection direction along the *b* axis. **e**, Zero-bias photocurrent along the *b* direction of a typical device in **d**, which is collected under the same illumination conditions as in **b**. (4,4-DFPD)₂Pbl₄ is poled into the P' state via the two electrodes along *a* direction beforehand. During the measurement of photocurrent, the poling terminals are open. **f**, Proposed scheme of σ^{+}/σ^{-} -induced electron-hole generation along the G-Y direction based on the experimental observations in **e**. I_1 and I_2 indicate the current generated from σ^{+}/σ^{-} light, respectively. **g**, Helicity-dependent photocurrent at different azimuthal angles θ in a four-terminal device. The signals are collected along the *b* direction under illumination of a 405-nm laser with light polarization modulated following the sequence $\sigma^{\circ} \rightarrow \sigma^{+} \rightarrow \sigma^{\circ} \rightarrow \sigma^{-}$ for two periods and the incident angle α fixed at -45° . **h**, Spectral evolution of the photocurrent in a four-terminal device for two different illumination wavelengths (405 nm and 515 nm). The signals are collected along the *b* direction with incident angle α of -45° and azimuthal angle θ of 90°. **i**, Proposed scheme of wavelength-dependent photoexcitation based on the experimental observation in **h**.

illumination light is linearly polarized (rotation angle of QWP φ =0°, 90°, 180°...), which corresponds to the linear photogalvanic effect (LPGE). The total measured signal, $I_l(\varphi)$, including both CPGE and LPGE current, can be expressed as^{37,38}

$$I_l(\varphi) = C\sin 2\varphi + L\sin 4\varphi + D\cos 4\varphi + A, \tag{4}$$

where l represents the measured direction (l=x or a in Fig. 3b for instance). The coefficient C ($C=(I_1-I_2)/2$) associated with the 2φ term characterizes CPGE, and L and D, associated with the 4φ terms and A, describe LPGE (A also contains possible contributions from some other effects, such as the Dember effect, the photovoltaic effect at contacts and the photon drag effect^{37,39}). The fitting results

of Fig. 4b,e show that C is close to 0 (<0.01 pA) along the a axis and C is -0.32 pA along the b axis, correspondingly. It should be noted that a constant photocurrent on the level of several picoamperes has been subtracted throughout for clarity; this does not affect the fitting of parameters except A (a typical example of the unsubstracted data is shown in Supplementary Fig. 15).

The values of the CPGE and LPGE coefficients (C, L and D) depend on several experimental parameters (the incident angle α , azimuthal angle θ , polarization state of the (4,4-DFPD)₂PbI₄ crystal) and CPGE and LPGE tensors of (4,4-DFPD)₂PbI₄ (ref. ⁴⁰). To figure out the detailed value of elements in the symmetry tensor of (4,4-DFPD)₂PbI₄, we conducted a series of measurements as shown in Fig. 4g. The incident angle α is fixed to be -45° and the azimuthal

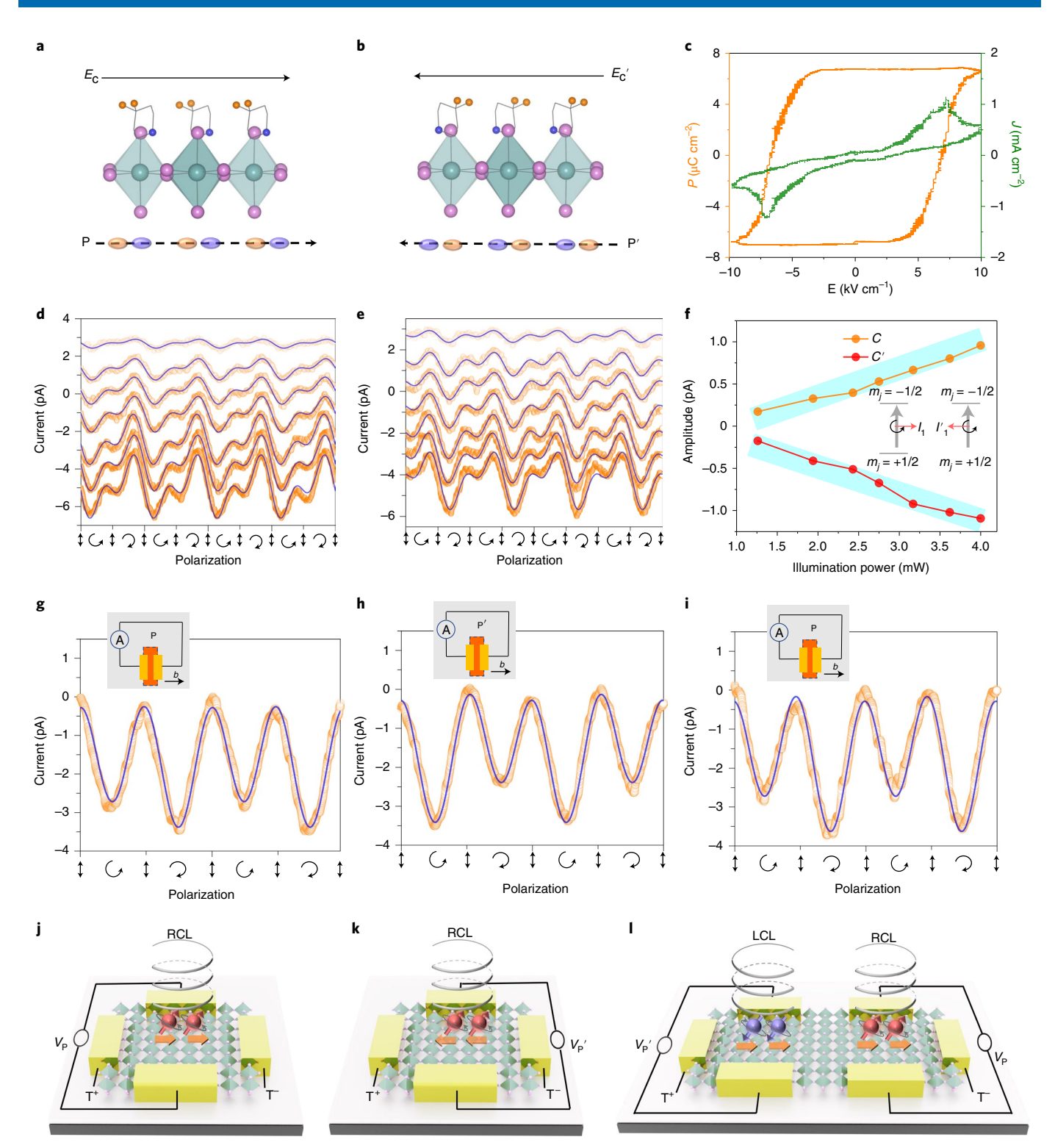


Fig. 5 | Room-temperature ferroelectrically switchable CPGE. a, The P state in a $(4,4\text{-DFPD})_2\text{Pbl}_4$ single crystal via electrical poling by an external electric field E_c . **b**, The P' state via electrical poling by an external electric field E_c' . **c**, Polarization–electric field (P-E) loop (left vertical axis) and its corresponding photocurrent density–electric field (J-E) scan (right axis) of a $(4,4\text{-DFPD})_2\text{Pbl}_4$ single crystal. **d**, Zero-bias photocurrents measured along the b direction under the illumination of a 405-nm laser with different power for the P polarized state. The laser power ranges from 4 mW to 1.26 mW (from bottom to top). For illustration, the curves are vertically shifted in steps of 1 pA. The incident angle α is -45° and the azimuthal angle θ is 90°. **e**, Zero-bias photocurrents measured along the b direction under the illumination of a 405-nm laser with different powers for the P' polarized state. **f**, CPGE coefficient versus illumination power curves. C corresponds to the P polarized state and C' to the P' state. **g-i**, Repeatedly electrically switchable CPGE in a four-terminal device following the sequence of $P \rightarrow P' \rightarrow P$ (**g,h,i**). The zero-bias signals are collected along the b direction with a light incident angle α of -45° and an azimuthal angle θ of 90°. **j,k**, Schematics of the transport of spin-down electrons under the illumination of σ^+ for P polarization (**j**) and P' polarization (**k**) in (4,4-DFPD)₂Pbl₄, corresponding to the observations in **g** and **h**, respectively. **l**, Manipulation of spin states via the corresponding ferroelectric domains of P and P' in one crystal.

angle θ is changed from 45° to 90° in steps. In the theory of CPGE and LPGE, C is related to a second-rank pseudo tensor β_{lm}^C and L and D are related to a third-rank tensor β_{lmn}^L (l, m and n denote directions in real space). Based on the $C_{2\nu}$ point group of (4,4-DFPD)₂PbI₄ (ref. ⁴⁰), the CPGE component $J_{\nu, \text{CPGE}}(\varphi)$ can be formulated as follows (the total photocurrent density $J_{\nu}(\varphi)$ is discussed in detail in Supplementary Discussion 3 and Supplementary Tables 1 and 2):

$$J_{y, \text{ CPGE}}(\varphi) = -\cos\alpha \sin 2\varphi \beta_{yz}^{C} I, \qquad (5)$$

where I is light intensity. According to equation (5), $J_{\scriptscriptstyle p \sim \rm PGE}(\varphi)$ is azimuthal angle-independent, which is consistent with our experimental observations (details are provided in Supplementary Fig. 16 for the comparison between the theoretical and experimental results). The prevailing term β_{yz}^C for the second-rank pseudo tensor indicates substantial spin splitting of the band structure along the y direction, in other words, along the b axis of (4,4-DFPD)₂PbI₄. This is as expected, because the a axis is the ferroelectric polarization direction. It is worth mentioning that the measured intrinsic CPGE coefficient β_{yz}^C of (4,4-DFPD)₂PbI₄, on the order of $10^{-7} \, {\rm V}^{-1}$, is comparable to that of tellurium $(3 \times 10^{-8} \, {\rm V}^{-1})$, the highest one reported^{40,41}.

To check the CPGE for near-band-edge excitation, we conduct further light polarization-dependent optoelectronic measurements for the four-terminal device with an excitation wavelength of 515 nm. Figure 4h shows the helicity-dependent photocurrent for two different illumination wavelengths. An above-gap wavelength (405 nm, used mostly in this work unless otherwise noted) and a near-gap wavelength (515 nm, corresponding to 2.41 eV, which is close to the bandgap of (4,4-DFPD)₂PbI₄, are utilized. The related coefficients of C, L, D and A are extracted from these measured curves (Supplementary Table 3 and Supplementary Fig. 17). We find that the fitted CPGE coefficient C is negative when the illumination source is 405 nm, but it becomes positive when the illumination source changes to 515 nm. The sign-reversed CPGE coefficients for these two wavelengths indicate that the mechanistic picture for optical selection of σ^+/σ^- at the relevant valleys is switched. Indeed, DFT calculation results (Supplementary Fig. 18) show that the band immediately above the lowest conduction band has opposite spin textures. Figure 4i shows the schematic structure with the relevant optical excitations derived by Fig. 4h. Specifically, when the wavelength is 515 nm, along the $+k_{\nu}$ direction, the absorption of σ^+ from VBM to CB1 involving $m_{j_{\perp}VBM} = +1/2$ to $m_{j_{\perp}CB1} = -1/2$ is first-order allowed, whereas the absorption of σ^+ in the $-k_{\nu}$ valley is first-order forbidden. Specifically, when the wavelength is 405 nm, along the $+k_{\nu}$ direction, the absorption of σ^+ from VBM to CB2 involving $m_{j_{\text{LVBM}}} = -1/2$ to $m_{j_{\text{LCB2}}} = +1/2$ is first-order forbidden, while the absorption of σ^+ in the -k, valley is first-order allowed.

As a ferroelectric crystal, switching the polarization direction of its domain would switch the spin-polarized electronic band structure. For example, the spin-up band in the $+k_y$ direction near the CBM can be switched to the spin-down band simply by poling the crystal polarization from the a direction to the -a direction. To reveal such feature, CPGE tests on the four-terminal device can be applied: a switching of photocurrent sign along the $+k_y$ direction under two opposite polarization states (P state with the dipole moment along [100] (as shown in Fig. 5a,b) would indicate the switching of the relevant spin-polarized band structure.

To demonstrate the reversibility of the polarization states in $(4,4\text{-DFPD})_2\text{PbI}_4$ single crystals, we conducted a polarization–electric field loop (P-E loop) measurement on a single $(4,4\text{-DFPD})_2\text{PbI}_4$ crystal with a double-wave method (Fig. 5c). A saturated polarization strength of ~7 μC cm⁻² can be realized when the maximum poling field is $10\,\text{kV}$ cm⁻¹. The distinctive current peaks corresponding to the ferroelectric domain switching can be clearly observed in

the J-E scan (right axis, Fig. 5c). The onset electric fields of ferroelectric switching of the observed P-E loop and J-E scan (first scan) are the same. The shape of the J-E curve is consistent with the switching behaviour of single-crystalline multidomain ferroelectrics. Supplementary Fig. 19 shows the pristine strip-like ferroelectric domains with a width of several tens to hundreds of nanometres of a single $(4,4-DFPD)_2PBI_4$ crystal.

Figure 5d,e show the zero-bias photocurrents under the illumination of a 405-nm laser with different powers for the P state and P' state, respectively. The blue solid curves are fitted results based on equation (4) and the related fitted coefficients (C, C', L, L', D, D')versus light intensities are provided in Fig. 5f and Supplementary Fig. 20. As we can see, the CPGE coefficient is positive for the polarization state P and it becomes negative when the polarization state switches to P' via an external poling field (Fig. 5f). The amplitude of the CPGE coefficient increases nearly linearly with the illumination power, which is reasonable, because CPGE is a second-order response to the light electric field42. The LPGE coefficients also follow a nearly linear relationship with the illumination power (Supplementary Fig. 20a). However, there is no obvious tendency for D and D', because their magnitudes are too small to draw conclusions (Supplementary Fig. 20b). The switchable CPGE in (4,4-DFPD)₂PbI₄ has been found to exist for different devices (Supplementary Fig. 21). For a single device, the switching behaviour is presented in Fig. 5g-i. Figure 5g displays the zero-bias photocurrent for the P polarized state and the device configuration is shown in Fig. 5j. Excited electrons with spin up/down will flow to the right/left electrode (marked as T-/T+) when illuminated with σ^+/σ^- light, resulting in a positive CPGE coefficient. As the polarization state of the channel material is converted into the P' state by an external electrical field E'_{c} (Fig. 5k), the relative magnitudes of the σ^+/σ^- photocurrent are reversed (Fig. 5h). Here, there is a sign reversal for the CPGE coefficient. Furthermore, the P state can be recovered again by a poling electrical field E_c (Fig. 5i). These demonstrations show that the electrical control of the spin degree of freedom in this 2D halide perovskite in a non-volatile manner has been realized (as summarized in Fig. 51).

In conclusion, we show the existence of persistent spin helix in (4,4-DFPD)₂PbI₄, with the unidirectional internal magnetic field linearly dependent on the crystal momentum along the [010] direction. By means of a ferroelectric field, we experimentally demonstrate the switching of spin texture, manifested by the switchable CPGE, at room temperature in a non-volatile manner. Achieving ferroelectric field control on the spin degree of freedom at room temperature in a system hosting the persistent spin helix not only underlines the importance of materials symmetry in designing exotic properties, but also suggests a promising route towards designing practical spintronic devices.

Online content

Any methods, additional references, Nature Research reporting summaries, source data, extended data, supplementary information, acknowledgements, peer review information; details of author contributions and competing interests; and statements of data and code availability are available at https://doi.org/10.1038/s41566-022-01016-9.

Received: 24 May 2020; Accepted: 26 April 2022; Published online: 02 June 2022

References

- Ohno, H. et al. Electric-field control of ferromagnetism. Nature 408, 944–946 (2000).
- Wunderlich, J. et al. Spin Hall effect transistor. Science 330, 1801–1804 (2010).
- Wang, K. L. et al. Electric-field control of spin-orbit interaction for low-power spintronics. Proc. IEEE 104, 1974–2008 (2016).

- Jiang, M., Asahara, H., Sato, S., Ohya, S. & Tanaka, M. Suppression of the field-like torque for efficient magnetization switching in a spin-orbit ferromagnet. *Nat. Electron.* 3, 751–756 (2020).
- Huai, Y. Spin-transfer torque MRAM (STT-MRAM): challenges and prospects. AAPPS Bulletin 18, 33–40 (2008).
- Kawahara, T., Ito, K., Takemura, R. & Ohno, H. Spin-transfer torque RAM technology: review and prospect. Microelectron. Reliab. 52, 613–627 (2012).
- Dietl, T. A ten-year perspective on dilute magnetic semiconductors and oxides. Nat. Mater. 9, 965–974 (2010).
- Dietl, T. & Ohno, H. Dilute ferromagnetic semiconductors: physics and spintronic structures. Rev. Mod. Phys. 86, 187 (2014).
- Jungfleisch, M. B., Zhang, W. & Hoffmann, A. Perspectives of antiferromagnetic spintronics. *Phys. Lett. A* 382, 865–871 (2018).
- Maruyama, T. et al. Large voltage-induced magnetic anisotropy change in a few atomic layers of iron. Nat. Nanotechnol. 4, 158–161 (2009).
- Shiota, Y. et al. Induction of coherent magnetization switching in a few atomic layers of FeCo using voltage pulses. Nat. Mater. 11, 39–43 (2012).
- 12. Datta, S. & Das, B. Electronic analog of the electro-optic modulator. *Appl. Phys. Lett.* **56**, 665–667 (1990).
- Winkler, R., Papadakis, S., De Poortere, E. & Shayegan, M. Spin-Orbit Coupling in Two-Dimensional Electron and Hole Systems (Springer, 2003).
- Žutić, I., Fabian, J. & Sarma, S. D. Spintronics: fundamentals and applications. Rev. Mod. Phys. 76, 323 (2004).
- Bychkov, Y. & Rashba, E. Properties of a 2D electron gas with lifted spectral degeneracy. J. Exp. Theor. Phys. Lett. 39, 78–81 (1984).
- Manchon, A., Koo, H. C., Nitta, J., Frolov, S. & Duine, R. New perspectives for Rashba spin–orbit coupling. Nat. Mater. 14, 871–882 (2015).
- Stranks, S. D. & Plochocka, P. The influence of the Rashba effect. *Nat. Mater.* 17, 381–382 (2018).
- Lee, H., Im, J. & Jin, H. Emergence of the giant out-of-plane Rashba effect and tunable nanoscale persistent spin helix in ferroelectric SnTe thin films. *Appl. Phys. Lett.* 116, 022411 (2020).
- Autieri, C., Barone, P., Sławińska, J. & Picozzi, S. Persistent spin helix in Rashba–Dresselhaus ferroelectric CsBiNb₂O₇. Phys. Rev. Mater. 3, 084416 (2019).
- Koralek, J. D. et al. Emergence of the persistent spin helix in semiconductor quantum wells. *Nature* 458, 610–613 (2009).
- Walser, M., Reichl, C., Wegscheider, W. & Salis, G. Direct mapping of the formation of a persistent spin helix. Nat. Phys. 8, 757–762 (2012).
- Ohno, M. & Yoh, K. Vanishing of inhomogeneous spin relaxation in InAs-based field-effect transistor structures. *Phys. Rev. B* 75, 241308 (2007).
- Nitta, J., Akazaki, T., Takayanagi, H. & Enoki, T. Gate control of spin-orbit interaction in an inverted In_{0.53}Ga_{0.47}As/In_{0.52}Al_{0.48}As heterostructure. *Phys. Rev. Lett.* 78, 1335–1338 (1997).
- Zhang, H.-Y. et al. Observation of vortex domains in a two-dimensional lead iodide perovskite ferroelectric. J. Am. Chem. Soc. 142, 4925–4931 (2020).

 Zhai, Y. et al. Giant Rashba splitting in 2D organic-inorganic halide perovskites measured by transient spectroscopies. Sci. Adv. 3, e1700704 (2017).

- Hong, X., Ishihara, T. & Nurmikko, A. Dielectric confinement effect on excitons in PbI₄-based layered semiconductors. *Phys. Rev. B* 45, 6961–6964 (1992).
- Wang, S., Huang, M., Wu, Y. N. & Chen, S. Absolute volume deformation potentials of inorganic ABX₃ halide perovskites: the chemical trends. *Adv. Theory Simulations* 4, 2100060 (2021).
- Frost, J. M. et al. Atomistic origins of high-performance in hybrid halide perovskite solar cells. *Nano Lett.* 14, 2584–2590 (2014).
- Dar, M. I. et al. Origin of unusual bandgap shift and dual emission in organic-inorganic lead halide perovskites. Sci. Adv. 2, e1601156 (2016).
- Wright, A. D. et al. Electron–phonon coupling in hybrid lead halide perovskites. *Nat. Commun.* 7, 11755 (2016).
- Chen, Z. et al. Remote phononic effects in epitaxial Ruddlesden-Popper halide perovskites. J. Phys. Chem. Lett. 9, 6676-6682 (2018).
- Guo, Z., Wu, X., Zhu, T., Zhu, X. & Huang, L. Electron-phonon scattering in atomically thin 2D perovskites. ACS Nano 10, 9992–9998 (2016).
- Chen, T. et al. Origin of long lifetime of band-edge charge carriers in organic-inorganic lead iodide perovskites. *Proc. Natl Acad. Sci. USA* 114, 7519–7524 (2017).
- Booker, E. P. et al. Formation of long-lived color centers for broadband visible light emission in low-dimensional layered perovskites. *J. Am. Chem. Soc.* 139, 18632–18639 (2017).
- Fu, Y. et al. Multicolor heterostructures of two-dimensional layered halide perovskites that show interlayer energy transfer. *J. Am. Chem. Soc.* 140, 15675–15683 (2018).
- 36. Harris, D. C. & Bertolucci, M. D. Symmetry and Spectroscopy: an Introduction to Vibrational and Electronic Spectroscopy (Courier Corporation, 1989).
- Ganichev, S. D. & Prettl, W. Spin photocurrents in quantum wells. J. Phys. Condens. Matter 15, R935 (2003).
- Osterhoudt, G. B. et al. Colossal mid-infrared bulk photovoltaic effect in a type-I Weyl semimetal. *Nat. Mater.* 18, 471–475 (2019).
- Gibson, A. & Kimmitt, M. Photon drag detection. *Infrared Millimeter Waves* 3, 181–217 (1980).
- Sturman, B. I. & Fridkin, V. M. Photovoltaic and Photo-Refractive Effects in Noncentrosymmetric Materials (Routledge, 2021).
- Belinicher, V., Ivchenko, E. & Sturman, B. Kinetic theory of the displacement photovoltaic effect in piezoelectrics. Zh. Eksp. Teor. Fiz. 83, 649–661 (1982).
- Quereda, J. et al. Symmetry regimes for circular photocurrents in monolayer MoSe₂. Nat. Commun. 9, 3346 (2018).

Publisher's note Springer Nature remains neutral with regard to jurisdictional claims in published maps and institutional affiliations.

© The Author(s), under exclusive licence to Springer Nature Limited 2022

Methods

Sample preparation. PbI₂, 4,4-difluoropiperidinium hydrochloride (97%), DMSO and HI solution (47 wt% in water) were purchased from Sigma-Aldrich. We grew (4,4-DFPD)₂PbI₄ single crystals according to the method in ref. ²⁴. In detail, 1.15 g PbI, (2.5 mmol) and 0.79 g 4,4-difluoropiperidinium hydrochloride (5 mmol) were placed in a 50-ml round-bottom flask with 25 ml of HI solution. The solution was then heated to 393 K in an oil bath for 1 h to fully dissolve all precursors (a condenser pipe was needed for reflux). On slowly cooling the solution at a rate of 0.1 K min⁻¹ to room temperature, we obtained orange (4,4-DFPD)₂PbI₄ crystals in large amounts. The 2D (4,4-DFPD)₂PbI₄ crystals were used for the following characterizations and tests: XRD, temperature-resolved PL, temperature-dependent/fluence-dependent TRPL, P-E loop and most CPGE measurements. For the absorption spectrum, thin (4,4-DFPD)₂PbI₄ films were used. For the solution used to prepare (4,4-DFPD), PbI4 film, as-grown (4,4-DFPD)₂PbI₄ single crystals were fully dissolved in DMSO to form a saturated solution. Stirring helped to speed up the dissolving process. Subsequently, the solution was spin-coated on an oxygen-plasma-pretreated glass substrate. Ramping speed and time could be adjusted to obtain films with different thicknesses. The coated film was then annealed on a hotplate at 100 °C for 10 min for further use. For the device used in CPGE measurements, the (4,4-DFPD)₂PbI₄ crystals were transferred onto an insulating glass substrate. Four electrodes (for four-terminal devices) or two electrodes (for two-terminal devices) were made using conductive silver paint (Ted Pella) with a polydimethylsiloxane mould or gold with shadow masks via electron-beam evaporation. The channel length along the b axis of (4,4-DFPD)₂PbI₄ could be controlled from 100 to 300 µm or even shorter (with shadow masks).

XRD and microscopy characterizations. XRD was conducted on a Panalytical X'Pert PRO MPD system equipped with a Cu K α source and a PIXcel solid-state line detector. The morphology of the $(4,4\text{-DFPD})_2\text{PbI}_4$ crystals was characterized by a Nikon Eclipse Ti-S inverted optical microscope. Scanning electron microscopy (SEM) images were collected on a Zeiss SUPRA 55 instrument at 2 kV with a forward-scatter detector. EBSD was conducted in a Karl Zeiss Ultra 1540 EsB SEM-FIB system equipped with a NordlysNano detector from Oxford Instruments. A 10-kV electron beam was used to obtain a spatial crystallographic orientation map of a $(4,4\text{-DFPD})_2\text{PbI}_4$ single crystal. The crystallographic orientation data were collected and analysed using Aztec software from Oxford Instruments.

Optical characterizations. The PL measurements were conducted on a customized system (a Nikon Eclipse Ti-S inverted optical microscope, a Thorlabs 4 Megapixel Monochrome Scientific charge coupled device camera and a Princeton Instruments SP-2358 spectrograph). A (4,4-DFPD) $_2\text{PbI}_4$ single crystal was excited using a Picoquant 405-nm pulsed diode laser, the power of which could be adjusted. For cryogenic PL, an INSTEC HCS302 microscope cryostat was used to hold the sample. Absorption spectra were measured using a Perkin Elmer Lambda 950 UV–vis–NIR spectrophotometer with a Photomultiplier R6872 detector at room temperature in air.

CPGE measurements. A continuous-wave diode laser operating at a wavelength of 405 nm (Thorlabs) was used as the excitation source. The laser beam had an average diameter of 4 mm so it could illuminate the whole (4,4-DFPD)₂PbI₄ single crystal between the electrodes of the device. In this case, the measurement error due to the spatially dispersive effect could largely be avoided⁴³. In these measurements, the laser power could be adjusted between 0 and 4.0 mW. In most experiments, the maximum power was utilized (the corresponding light intensity was 31.8 mW cm⁻²). Another diode laser (515 nm) was used for wavelength-dependent CPGE, for comparison with the 405-nm wavelength. A QWP was used to modulate the light polarization by rotating the angle between the fast axis of the QWP and the polarization direction of incident light. The rotation procedure of the QWP was controlled by a motor (K-Cube Brushless DC Servo Driver, Thorlab). There were two kinds of QWP (Thorlabs): a zero-order 405-nm QWP for the 405-nm light source and an achromatic 350-850-nm QWP for the 515-nm light source. I-t curves were recorded using an Autolab PGSTAT302N potentiostat. All CPGE measurements were performed at room temperature.

P-E loop measurements. The double-wave method was used to measure the P-E loop of $(4,4\text{-}\mathrm{DFPD})_2\mathrm{PbI}_4$ single crystals. A two-terminal device containing a $(4,4\text{-}\mathrm{DFPD})_2\mathrm{PbI}_4$ single crystal was tested. An electric field with an amplitude of $\pm 10\,\mathrm{kV}\,\mathrm{cm}^{-1}$ and an operating frequency of 1 Hz was generated by a Tektronix AFG1022 arbitrary function generator together with a MATSUSADA AP-1B3(A) high-voltage amplifier. The measurement was conducted at 363 K in air because this speeds up the dipole switching process, kinetically⁴⁴. Similarly, polarization switching manipulations for $(4,4\text{-}\mathrm{DFPD})_2\mathrm{PbI}_4$ single crystals during CPGE measurements were achieved in a similar way but via an a.c. + d.c. method⁴⁵. The electric field used in d.c. poling was +10 kV cm $^{-1}$ / $-10\,\mathrm{kV}\,\mathrm{cm}^{-1}$ for the two different polarized states and lasted for 10s each time.

 $\label{eq:DFT} \textbf{DFT calculations.} \ All \ first-principles \ calculations \ were \ performed \ using \ the \ JDFTx \ plane-wave \ DFT \ software^{46}. \ The \ Perdew-Burke-Ernzerhof \ (PBE)$

exchange-correlation functional47 was used in conjunction with the DFT-D2 dispersion correction48 to account for the long-range interactions between the molecular components of this hybrid structure. Fully relativistic pseudopotentials⁴⁹ were used for all atoms within the unit cell to accommodate the use of SOC, and the plane-wave energy cutoff was set to 810 eV. A structural relaxation was performed iteratively with these settings to optimize the lattice constants and atomic positions. Self-consistent calculations were performed using a coarse Gamma-centred mesh of $4 \times 4 \times 4$ *k*-points to compute the electronic band structure and density of states. After performing electronic structure calculations, all quantities were transformed into the maximally localized Wannier function basis50. A total of 380 Gaussian Wannier centres were iteratively fitted to the band structure in the energy range $-25.7 \,\text{eV}$ to $+7.75 \,\text{eV}$, relative to the VBM. This fitting allowed for interpolation to a much finer k-mesh than originally used. Specifically, using the converged Wannier functions, energy and spin values were calculated for the split VBM and CBM bands using a $16 \times 16 k$ -point mesh in each 2D plane, from which spin texture could be plotted explicitly and internal magnetic field calculated using the energy split between consecutive bands.

Data availability

The data supporting the findings of this study are available within the paper.

Code availability

Codes are available upon reasonable request from the corresponding authors.

References

- Ji, Z. et al. Spatially dispersive circular photogalvanic effect in a Weyl semimetal. Nat. Mater. 18, 955–962 (2019).
- 44. Jin, L., Li, F. & Zhang, S. in *Progress in Advanced Dielectrics* (ed Jin, L.) Ch. 2, 21–104 (World Scientific, 2020).
- Hong, C. et al. Enhanced piezoelectric and dielectric properties of Pb (Yb_{1/2}Nb_{1/2})O₃-Pb (Mg_{1/3}Nb_{2/3})O₃-PbTiO₃ crystals by combining alternating and direct current poling. *J. Appl. Phys.* 129, 124101 (2021).
- Sundararaman, R. et al. JDFTx: software for joint density-functional theory. SoftwareX 6, 278–284 (2017).
- Perdew, J. P., Burke, K. & Ernzerhof, M. Generalized gradient approximation made simple. *Phys. Rev. Lett.* 77, 3865–3868 (1996).
- Grimme, S. Semiempirical GGA-type density functional constructed with a long-range dispersion correction. *J. Comput. Chem.* 27, 1787–1799 (2006).
- Hamann, D. Optimized norm-conserving Vanderbilt pseudopotentials. Phys. Rev. B 88, 085117 (2013).
- Marzari, N. & Vanderbilt, D. Maximally localized generalized Wannier functions for composite energy bands. Phys. Rev. B 56, 12847–12865 (1997).

Acknowledgements

This work is supported by the US ARO under grant no. W911NF-21-1-0013 (J.S. and R.S.), the US AFOSR under award no. FA9550-18-1-0116 (J.S.), the US AFOSR under award no. FA9550-YR-1-XYZQ (Y.P.), the New York State's Empire State Development's Division of Science, Technology and Innovation through Focus Center contract no. C180117 (L.Z., J.S., Z.L. and T.M.L.) and the US National Science Foundation under award nos. 1706815 (J.S.), 2031692 (J.S.) and 1916652 (R.S. and J.S.).

Author contributions

J.S., R.S., Y.P. and L.Z. conceived and developed the idea. L.Z., Y.H., J.J. and J.S. planned the experiments. L.Z. and J.J. prepared samples and devices. L.Z. and J.J. performed optical and P.I. experiments. L.Z. performed ferroelectric polarization tests and SEM studies. L.Z. and J.J. performed CPGE measurements. C. Multunas, M.C., R.S., Y.P., C. Ming and Y.-Y.S. performed DFT calculations. Y.H. performed XRD and Z.L. performed EBSD. L.Z. processed the raw data. L.Z., C. Multunas, Y.P., R.S. and J.S. analysed and interpreted the results. L.Z. prepared the initial manuscript draft and J.S. revised it. All authors were involved in the discussion of data analysis and the writing of the manuscript. J.S., R.S. and Y.P. supervised the project.

Competing interests

The authors declare no competing interests.

Additional information

Supplementary information The online version contains supplementary material available at https://doi.org/10.1038/s41566-022-01016-9.

Correspondence and requests for materials should be addressed to Yuan Ping, Ravishankar Sundararaman or Jian Shi.

Peer review information *Nature Photonics* thanks Jean Luc Pelouard and the other, anonymous, reviewer(s) for their contribution to the peer review of this work.

Reprints and permissions information is available at www.nature.com/reprints.